Geophysical Journal International

Geophys. J. Int. (2014) **196,** 340–356
Advance Access publication 2013 October 19

doi: 10.1093/gji/ggt328

From earthquake size to far-field tsunami amplitude: development of a simple formula and application to DART buoy data

Emile A. Okal, Dominique Reymond and Hélène Hébert

Department of Earth and Planetary Sciences, Northwestern University, Evanston, IL 60208, USA. E-mail: emile@earth.northwestern.edu
[2]*Laboratoire de Géophysique, Commissariat à l'Energie Atomique et aux Energies Alternatives, Boîte Postale* 640, F-98713 *Papeete, Tahiti, French Polynesia*
[3]*Laboratoire de Détection et Géophysique, Commissariat à Energie Atomique et aux Energies Alternatives, Bruyères-le-Châtel,* F-91297 *Arpajon Cedex, France*

Accepted 2013 August 14. Received 2013 August 13; in original form 2013 August 1

SUMMARY

We derive a simple formula relating tsunami amplitude in the far field to seismic moment, distance and azimuth from propagating rupture. Our formula is obtained from a comparison of a set of 4650 Pacific-wide simulations, computed for a series of sources spread over 10 subduction zones and four order of magnitudes in seismic moments. Our simulations are run both for a real grid reproducing the true bathymetry of the Pacific Basin and for an idealized one featuring a constant depth of 4000 m and no shorelines. This enables us to study and model separately the influence on the final amplitude of a tsunami wave of effects such as directivity and irregular bathymetry. The contribution of source size directivity and propagation over the sphere are studied using the constant-depth simulations. The influence of distance does not require any dispersive term and is properly modelled by geometrical spreading on the sphere. The directivity term, described classically in the frequency domain by Ben-Menahem & Rosenman can be approximated in the time domain by a moment-dependent linear regression as a function of azimuth. Finally, and after an allowance is made for the effect of receiver bathymetry using Green's law, the effect of irregular bathymetry is found to be generally defocusing, and can be modelled as a linear regression with distance. Once an estimate of the seismic moment of the parent earthquake is known, and under the assumption of a subduction mechanism along a fault of known azimuth, the resulting formula allows to forecast far-field tsunami amplitudes on the high seas. We use a data set of 116 tsunami amplitudes recorded at 51 past and present DART buoys following 21 tsunamigenic events to compare the estimates predicted by our algorithm to the amplitudes actually recorded. The average values of the residuals are 0.00 ± 0.25 logarithmic units, and 0.02 ± 0.20 at distances greater than 20°. An important aspect of our algorithm is that it correctly predicts the DART amplitudes for the 2011 Tohoku tsunami (0.10 ± 0.15 logarithmic units), even though its region was not included when building the algorithm.

Key words: Tsunamis; Computational Seismology; Early warning; Pacific Ocean.

1 INTRODUCTION

Tsunami warning in the far field, notably in French Polynesia, remains largely based on the detection of a strong earthquake, and on the interpretation of its source in terms of tsunamigenic potential. The latter uses an evaluation of the seismic moment of the earthquake, measured at the lowest possible frequency.

In this context, it is important to be able to forecast, if possible based on solid theoretical grounds, the zero-to-peak amplitude η of the tsunami expected on a distant receiver shoreline, as a function of the seismic moment M_0 of the parent earthquake, in order to give a quantitative dimension to any ensuing tsunami alert. Along these lines, and more than 20 yr ago, Talandier & Okal (1989) had proposed the formula

$$\eta = 0.3\ M_0 \sqrt{\frac{90}{\Delta \cdot \sin \Delta}}, \tag{1}$$

where η was measured in centimetres, M_0 in units of 10^{27} dyn×cm and the epicentral distance Δ in degrees. This formula was based on an empirical optimization of a data set of synthetic waveforms, computed for a point source in the normal mode formalism introduced by Ward (1980). Talandier & Okal (1989) had shown that (1) provided an acceptable agreement with a data set of 17 tsunamis recorded on the maregraph operated in the Papeete harbour.

However, their study suffered from a simplistic approach, since it used a single optimized constant (0.3), a single receiver location and ignored such well-known physical effects as source directivity. In an operational context, Reymond *et al.* (2012) recently proposed a forecasting method based on the interpolation of a large database of pre-computed solutions, which follows the general approach of Titov *et al.* (2005). While the use of simulated solutions ensures in principle the incorporation of source and path effects affecting the final amplitude, their individual contributions are not directly identifiable. In this study, we take a different approach and seek a formula more precise than (1), based on a step-by-step algorithm following the successive influence of various parameters on the final amplitude of the wave. In this respect, the present approach can be regarded as complementary to that of Reymond *et al.* (2012). While not providing the same level of numerical sophistication, it remains closer to the physical agents governing the evolution of the wave's amplitude from source to receiver. We emphasize, however, that it cannot handle a detailed interaction with a coastline structure.

2 GENERAL REMARKS

In very general terms, the amplitude η observed at a distant receiver will be governed by the combination of several effects :

(1) A source effect, expressing the amplitude of the initial deformation η_0 of the sea level in the epicentral area. In principle, the latter should be proportional to the seismic slip along the dislocation, Δu. In the far field, the amplitude of the tsunami will result from the integration of η_0 over the source area, varying like the surface of faulting S, and therefore the primary effect of 'source size' on the field η should be a direct proportionality to the seismic moment M_0. We note that this simple result is of course in agreement with normal mode theory, which treats the tsunami as a particular case of the free oscillations of the Earth, and therefore of seismic waves, whose amplitudes depend linearly on seismic moment (Gilbert 1970; Ward 1980).

(2) However, source finiteness leads to azimuthal directivity, a classical effect first described for seismic surface waves by Ben-Menahem (1961), and extended to the case of tsunamis by Ben-Menahem & Rosenman (1972). For an earthquake whose rupture propagates linearly at velocity V_R along a fault of length L, the interference between elementary segments of the fault is expressed in the far field through a directivity function

$$D = \operatorname{sinc}\left[\frac{\omega L}{2\,c}\left(\frac{c}{V_R} - \cos\phi\right)\right], \qquad (2)$$

which multiplies the spectral amplitude of the tsunami in the azimuth ϕ measured from the direction of rupture, c being the phase velocity of the tsunami, ω the angular frequency and sinc the 'circular sine' function ($\operatorname{sinc} x = (\sin\, x)/x$). For a tsunami wave, and since V_R is always hypersonic with respect to c, the lobe of directivity is always directed at right angle to the fault rupture. In addition, and for a given frequency, the importance of the directivity effect grows with L, and hence with the size of the earthquake; in practice, it means that the lobe of directivity becomes narrower with increasing M_0 (Okal & Talandier 1991).

(3) Next, as the tsunami propagates a distance Δ from its source to the receiving shore, there will be an evolution of the vertical amplitude η of the displacement field of the ocean surface, in response to several phenomena.

Table 1. Source parameters used for hydrodynamic simulations.

Region	Centroid	Focal mechanism	SMALL				AVERAGE				BIG				MEGA			
	Lat., Lon. (°N, °E)	ϕ, δ, λ (°)	L, W (km)	Δu (m)	M_0 (10^{27} dyn×cm)	h (km)	L, W (km)	Δu (m)	M_0 (10^{27} dyn×cm)	h (km)	L, W (km)	Δu (m)	M_0 (10^{27} dyn×cm)	h (km)	L, W (km)	Δu (m)	M_0 (10^{27} dyn×cm)	h (km)
Kuril	46.95, 154.0	214, 15, 90	94, 42	1.52	3	18	200, 90	3.33	30	24	520, 160	7.2	300	33	1200, 300	16.7	3000	51
Kamchatka	53, 160.5	221, 20, 90	52, 25.5	1.52	1	15	113, 55	3.28	10	19	243, 118	7.0	100	30	600, 200	17	1000	44
Aleutian	51.3, −175.8	246, 22, 85	52, 26	1.55	1.04	15	113, 56	3.33	10.4	20	243, 120	7.17	104	32.5	600, 200	18	1040	47
Unimak	53.5, −163.2	243, 10, 90	50, 25	1.30	1	12.5	120, 60	2.78	10	15	210, 100	9.50	100	20	600, 220	15.2	1000	27
Alaska	58.7, −150	220, 20, 90	83, 28	1.72	2	14	179, 60	3.72	20	17	386, 129	8.03	200	28	980, 200	20.4	2000	40
Cascadia	46, −125	350, 15, 80	70, 35	1.22	1.5	13.5	163, 46	4	15	20	350, 100	8.6	150	27	1100, 150	18.2	1500	30
Peru	−16.38, −73.78	310, 18, 63	51.5, 25.5	1.52	1	14	111, 55	3.28	10	18.5	240, 118	7.1	100	28	800, 180	14	1000	38
Chile	−24.17, −70.74	354, 22, 90	83, 28	1.30	1.5	23	180, 60	2.78	15	29	388, 129	6	150	42	1160, 200	12.9	1500	55
Chile-South	−42, −74.2	8, 12, 90	100, 30	1.33	2	17	216, 65	2.85	20	21	464, 139	6.20	200	28	1000, 300	13.3	2000	45
Tonga	−19, −173.4	195, 30, 90	93, 28	1.08	1.4	17	200, 60	2.30	14	25	432, 130	5	140	43	1100, 200	12.7	1400	60

Note:For each model, h is the centroid depth of the source.

First, the tsunami will spread geometrically on the surface of the Earth, in the same fashion as a classical surface wave, whose amplitude varies like $1/\sqrt{\sin\Delta}$.

Second, the amplitude of the tsunami could be influenced by a dispersion of its various spectral components. This could be due to propagation at frequency-dependent velocities, outside the shallow-water approximation, which is comparable to the dispersion of classical seismic surface waves, for which phase-stationary asymptotics predict an amplitude decaying as $\sqrt{1/\Delta}$ (Okal 1989). This motivated Talandier & Okal (1989) in their formulation of eq. (1), but we will show that this term is actually unwarranted.

Finally, even under the shallow-water approximation, the non-linear nature of the hydrodynamic equations governing propagation can lead to an evolution of the waveshape. Even solitary waves can produce tails propagating at different speeds, resulting from 'amplitude dispersion', since strictly speaking, the shallow-water speed $\sqrt{g(H+\eta)}$ depends on the surface amplitude η of the wave. However, under conditions typical of even a major tsunami, this effect has been shown to be largely irrelevant for propagating distances less than the full perimeter of the Earth (Tadepalli & Synolakis 1996).

(4) More importantly, irregular bathymetry can strongly affect the amplitude η of the tsunami in the far field. In the shallow-water approximation, when the wavelength Λ is large with respect to the height H of the water column, the phase velocity $c = \sqrt{gH}$ depends on H, and the oceanic basin behaves as a medium of variable refraction index in geometrical optics, giving rise to focusing and defocusing effects (Satake 1987; Woods & Okal 1987).

(5) Finally, there will be a receiver effect, expressing the interaction of the wave with the coastal system. It will be totally controlled by the local, small-scale bathymetry of the receiver area, as well as by the topography of the initially dry land inundated by the tsunami. Even though such effects are now possible to model numerically, they must be analysed on a case by case basis, using small-scale bathymetric and topographic charts, and therefore cannot be modelled theoretically. As such, they will not be considered further in this study, which will be limited to the analysis of the amplitude η in deep water.

3 METHODOLOGY

Our approach consists of building a large database of numerical simulations of tsunami waves for sources located at the periphery of the Pacific Basin, whose geometries are representative of past tsunamis or of events which may happen in the future, and whose size spans several orders of magnitude in M_0. In practice, and as detailed in Table 1 and Fig. 1, we have identified 10 source regions, and for each of them, four levels of seismic moments M_0, referred to as 'SMALL', 'AVERAGE', 'BIG' and 'MEGA'. We specifically exclude the Japanese coastline from our region space, which provides us with the capability to run, in Section 5, an independent validation of our model by comparing data recorded during the 2011 Tohoku earthquake, with amplitudes estimated from our algorithm, derived using simulations from sources in other regions of the Pacific, and thus to verify the universal character of our approach.

The focal geometries used in the simulations are either derived from recent representative events in the various regions (e.g. in Region 7, Peru, we use the mechanism of the 2001 earthquake), or taken as low-angle thrust faulting, this choice being motivated by

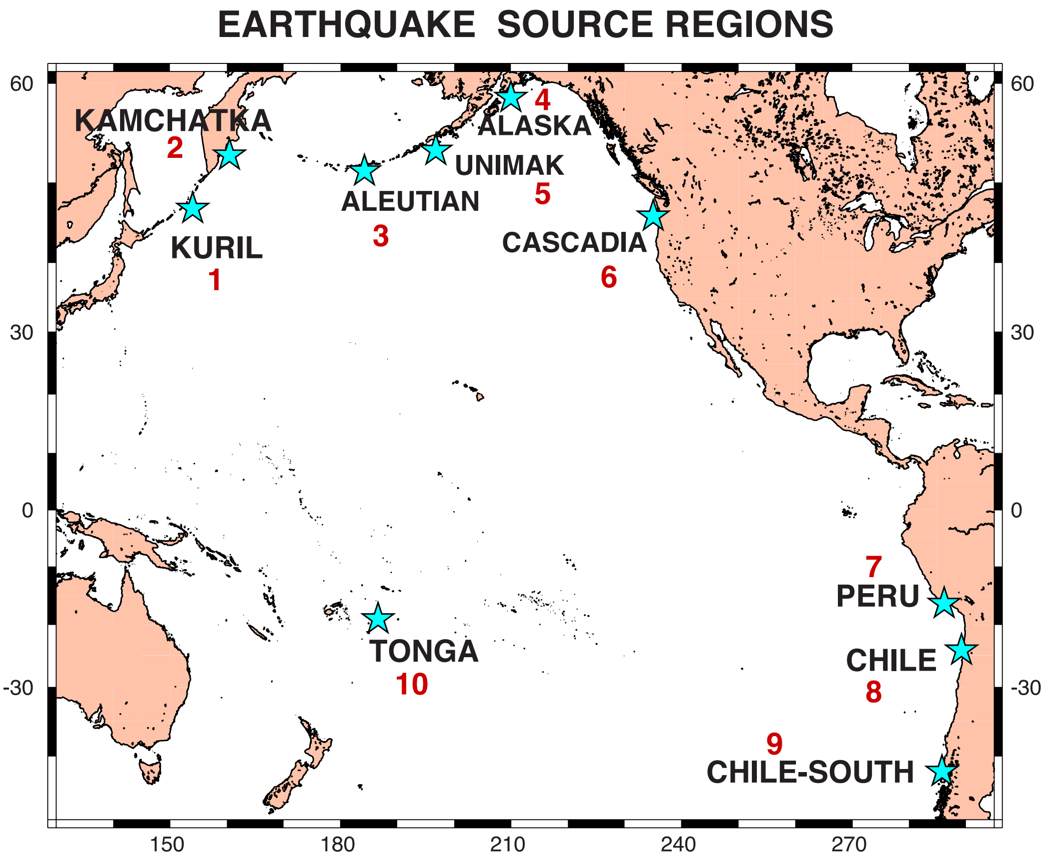

Figure 1. Map of the 10 source regions used in this study.

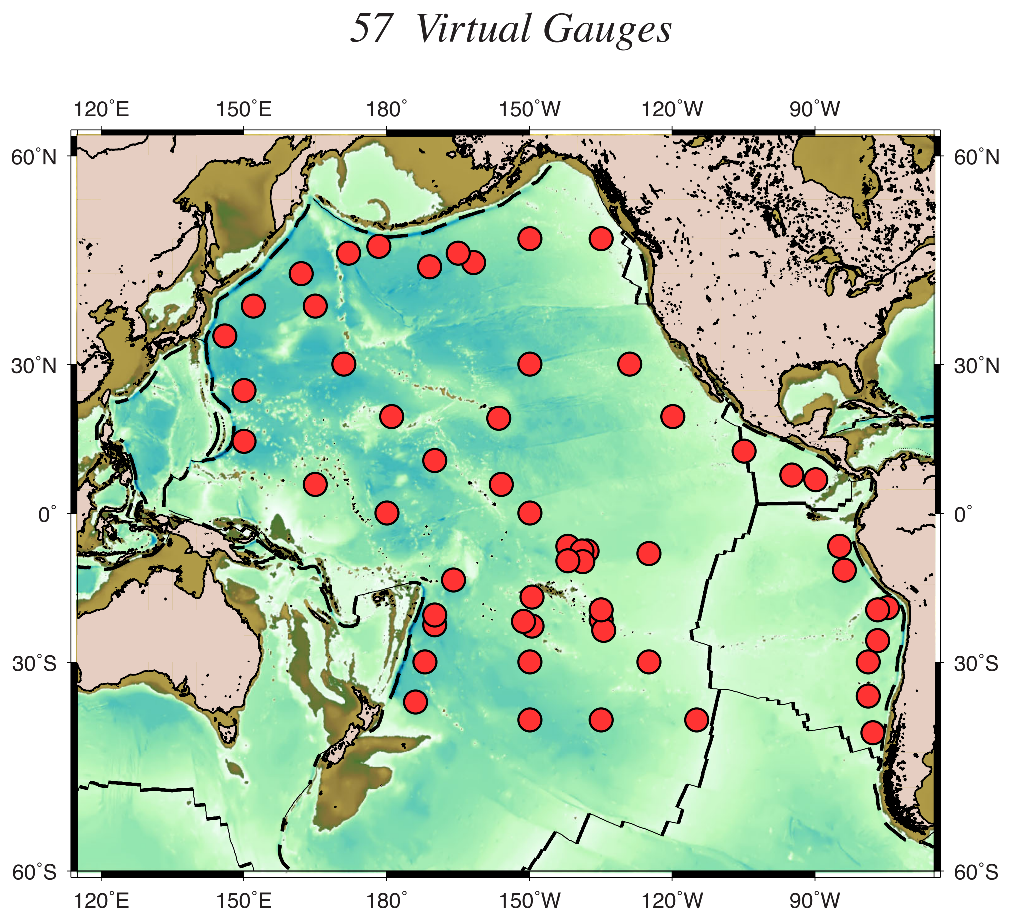

Figure 2. Map of the Pacific Basin, showing the location of the 57 virtual gauges used in this study.

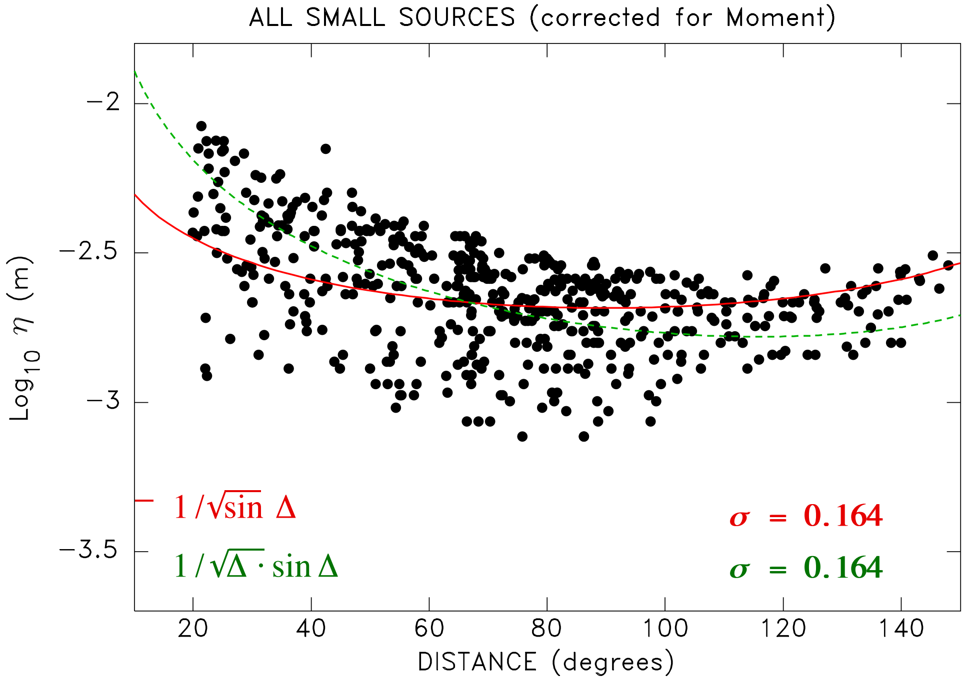

Figure 3. Amplitude η (plotted logarithmically) versus epicentral distance Δ simulated under Model 4000 (flat bathymetry) for the 'SMALL' class of sources. Only distances greater than 20° have been retained. Values of η have been corrected to a common moment. The solid line represents the best fit to a function of the type $1/\sqrt{\sin\ \Delta}$, the dotted one to $1/\sqrt{\Delta\ \cdot\ \sin\Delta}$. Note the similar values of the rms residuals of the fits.

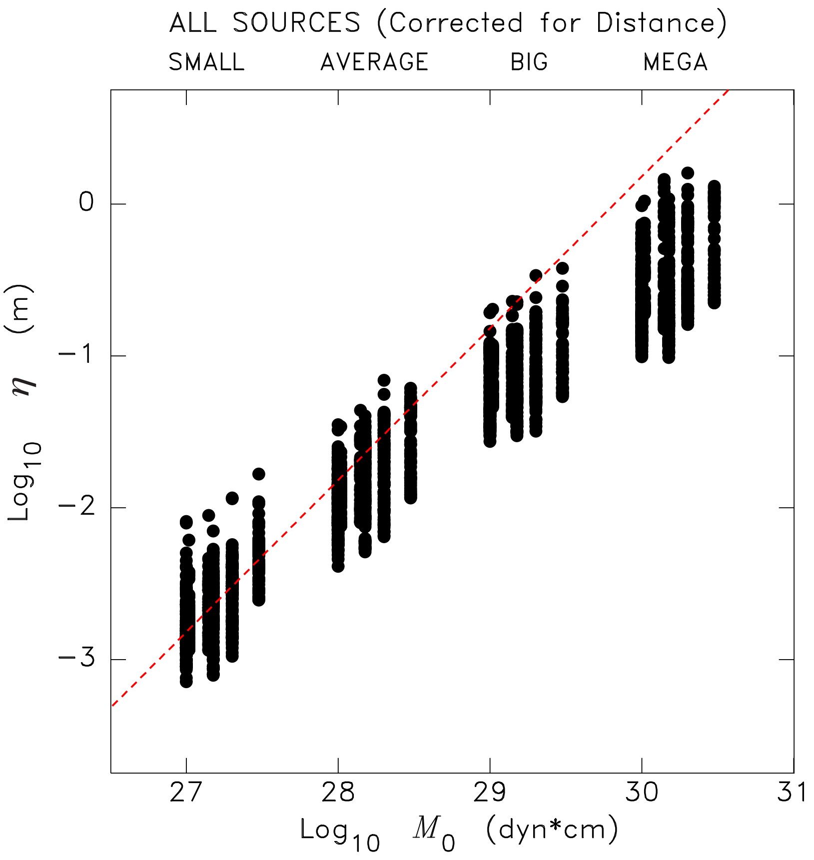

Figure 4. Simulated amplitude η versus seismic moment M_0, for the 40 sources considered in this study. The values of η have been multiplied by $\sqrt{\sin\Delta}$ to correct for geometrical spreading. The dashed line is the best fit with a (logarithmic) slope of 1 to the 'SMALL' group. Note that the other groups become increasingly deficient with respect to that fit, as the seismic moment increases, reflecting the effect of directivity due to source finiteness.

the fact that large tsunamis are overwhelmingly (but not exclusively) generated by such sources. Some discussion of the implication of this choice of mechanism will be given in Section 5.

For each of these 40 sources, we proceed through a simulation of the tsunami in the Pacific Basin for a total duration of 24 hr, using Hébert *et al.*'s (2001) code, originally developed by Guibourg *et al.* (1997). As a product of these simulations, we store into a database the maximum amplitude η at 57 virtual gauges spread over the Pacific Basin. Originally, their locations were selected in the vicinity of populated coastlines; in order to refine our analysis of directivity effects, we eventually included additional gauges in the centre of the basin (Fig. 2).

In addition, and in order to analyse the influence of focusing effects, we systematically repeated our simulations over an ocean model with a flat bottom ('Model 4000'), featuring a uniform depth $H_{4000} = 4000$ m. Consequently, the product of our simulations makes up a database of 4560 values of tsunami amplitudes η, which we will analyse to obtain an improved formula capable of replacing (1).

Table 1 lists the parameters of the 40 sources used. Their geometries were either obtained from recent events whose focal mechanisms have been published (e.g. in the GlobalCMT catalogue), or estimated from the kinematic parameters of the relevant plates. Source dimensions (fault length L, fault width W and slip Δu) are inspired from scaling laws (Geller 1976), with W bounded in the case of the larger moments (Scholz 1982). In very general terms, one of the sources in each subduction zone is meant to reproduce a known, historically documented tsunami; depending on the particular region, this may correspond to the 'BIG' scenario (e.g. Unimak, 1946) or to the 'MEGA' one (e.g. Southern Chile, 1960). Within each size class, our moments vary by a factor of 3 (e.g. from one to three times 10^{28} dyn×cm for the 'AVERAGE' class), and each class is offset from the next one by a factor of 10 in moment. This arrangement, rather than imposing fixed values of the moment in each class size, helps provide continuity with M_0 in the study of its control of the variation of η.

We further emphasize that not all levels of earthquake size used here are documented (or probable) in all selected zones. For example, no earthquakes of 'MEGA' or even 'BIG' class are documented in Tonga. Yet, the recent events in Sumatra (2004) and Japan (2011) have shown that the instrumented seismological record significantly undersamples the true level of seismicity in at least several subduction zones, to the extent that existing models aimed at predicting maximum earthquake size as a function of simple tectonic parameters (Ruff & Kanamori 1980) are now abandoned, in favour of a precautionary approach under which all subduction zones of sufficient length are now considered as having the potential for a 'MEGA' class event (McCaffrey 2007; Stein & Okal 2007).

3.1 The distance factor

In order to define a proper distance factor in η, we focus on the flat-bottom Model 4000, thus eliminating any effects due to focusing, and we consider only the 'SMALL' sources, for which the directivity due to source finiteness is minimized. Fig. 3 plots η (in logarithmic scale) versus distance Δ. Amplitudes have been normalized to a

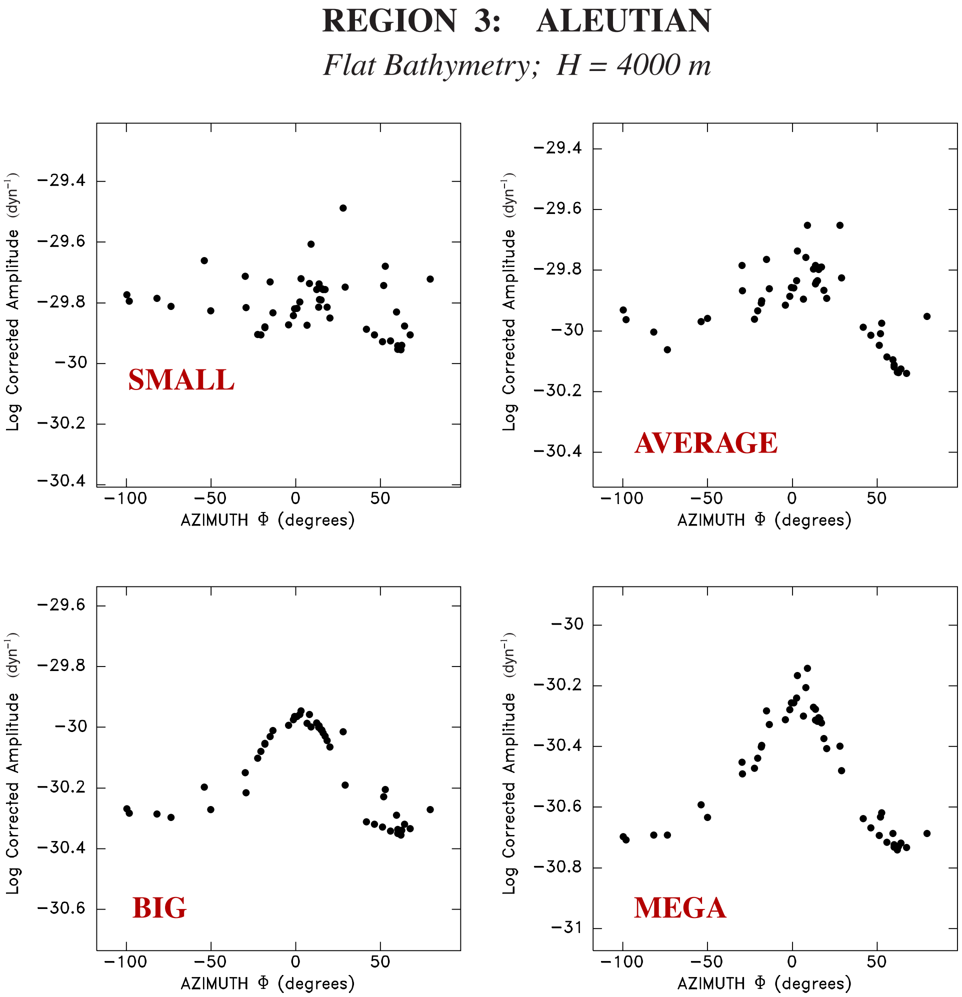

Figure 5. Amplitudes Z (after correcting for distance, and scaling to a constant moment) simulated in the case of Model 4000 for sources in the Aleutian region plotted as a function of receiver azimuth Φ, measured from the perpendicular to the fault strike. Receivers at $\Delta < 20°$ excluded. Note the growing effect of directivity as the size of the event increases.

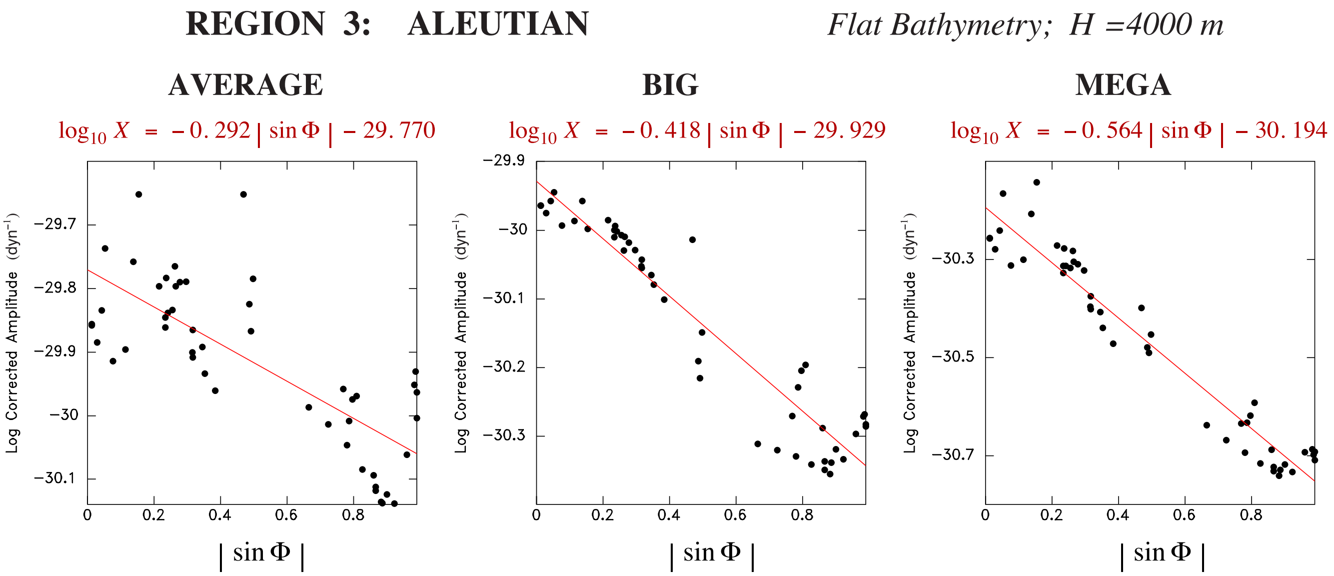

Figure 6. Empirical regression of the effect of directivity as a function of receiver azimuth illustrated in the case of region 3 (Aleutian). For each event size, the corrected amplitudes Z have been further corrected for distance and are plotted as a function of $|\sin\ \Phi|$ (see text for details). Each data set is then regressed linearly, with the results given in red. Note the increase in (absolute) slope, expressing narrowing of directivity lobes with earthquake size, as predicted by (2).

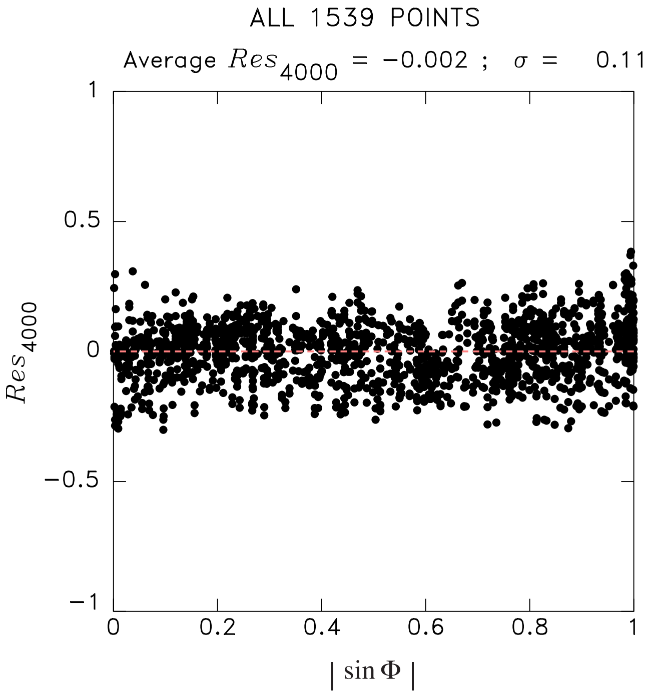

Figure 7. Performance of the directivity correction (5) tested on the 1539 AVERAGE, BIG and MEGA amplitudes simulated under Model 4000.

common moment (averaged geometrically to $\overline{M_0} = 1.44 \times 10^{27}$ dyn×cm), and all distances less than 20° excluded. The red solid line represents the best fit to the 513 values of η of a function proportional to $1/\sqrt{\sin\,\Delta}$ and the green dashed one to $1/\sqrt{\Delta \cdot \sin\,\Delta}$.

This figure cannot help discriminate between the two functions, given the identical rms residuals σ for the two fits (0.164 logarithmic units). Since the dispersed function $1/\sqrt{\Delta \cdot \sin\,\Delta}$ is difficult to justify theoretically, we will use the purely spherical geometric spreading $1/\sqrt{\sin\,\Delta}$.

3.2 Amplitude versus moment and the effect of source finiteness

We still consider the flat-bottom Model 4000, and now plot in Fig. 4 all simulated amplitudes versus seismic moment, after correcting for the effect of distance, as defined in the previous section. Specifically, the simulated amplitudes have been multiplied by $\sqrt{\sin\,\Delta}$. We note that the corrected amplitudes grow slower than expected from a strict proportionality to seismic moment, expressed in Fig. 4 as the dashed line with a (logarithmic) slope of 1. This systematic deficiency, which becomes exacerbated as M_0 increases, is due to the directivity effect described in (2).

In this context, we study in Fig. 5, in the example of the Aleutian source region, the variation of η as a function of the azimuth to the receiver. We plot in abscissa the angle $\Phi = \phi_f - \phi_R - \pi/2 = \phi - \pi/2$, where ϕ_R is the geographical azimuth to the receiver, ϕ_f the strike of the fault and ϕ the angle classically used in (2); as such, Φ measures the azimuth to the receiver, centred at right angle to the fault, on the lobe of maximum directivity. The amplitudes $Z = (\sqrt{\sin\,\Delta}\,/\,M_0) \cdot \eta$ are plotted in ordinate on a logarithmic scale after normalizing to a common value of the seismic moment, and correcting for distance. Receivers at epicentral distances less than 20° are excluded.

For the SMALL source, with its weak seismic moment and source dimensions, the amplitude shows no definite trend with azimuth, but for the larger sources, it features a directivity effect in the form of a bell-shaped curve whose width decreases regularly, from ‘AVERAGE’ through ‘BIG’ to ‘MEGA’, as theoretically predicted (Ben-Menahem & Rosenman 1972; Okal & Talandier 1991). It should be possible, at least in principle, to model this curve, in order to predict the directivity effect, especially for the largest events carrying a real transoceanic tsunami hazard.

However, formula (2) is expressed in the frequency domain and our goal is, eventually, to obtain an estimate of Z in the time domain. Its use would require targeting a particular frequency, which is unrealistic given the dependence of (2) on L, and the oscillatory nature of the sinc function, predicted to lead to holes in the theoretical spectra. We therefore adopt a more empirical approach, which consists of fitting the curves in Fig. 5 with a simple function of the angle Φ; this amounts, at least empirically, to defining a kind of time-domain expression of D, which can be thought of as a weighted integral of its theoretical values over frequency. In this context, we note the obvious curvature of $Z(\Phi)$ in Fig. 5, which suggests regressing against a non-linear function of Φ. Furthermore, this curvature (i.e. the width of the bell curves in Fig. 5) obviously depends on seismic moment, through the fault length L in (2), which suggests separate regressions for the various classes of events. We therefore proceed as follows:

(i) We first modify Fig. 5 by plotting $\log_{10} Z$ as a function of $|\sin\,\Phi|$. In practice, this linearizes significantly the azimuthal dependence of corrected amplitude (Fig. 6).

(ii) Then, for each source region, and for each of the three earthquake sizes ‘AVERAGE’, ‘BIG’ and ‘MEGA’, we regress linearly the values of $\log_{10} Z$ versus $|\sin\,\Phi|$, in the form

$$\log_{10}\,Z = a \cdot |\sin\,\Phi| + b, \tag{3}$$

with the results shown as the straight lines in Fig. 6 in the example of Region 3 (Aleutians). We exclude the ‘SMALL’ group for which the effect of directivity remains negligible. The 30 values of a (slope) and b (zero-intercept) are in turn regressed against $\log_{10} M_0$ as

$$a = \alpha \cdot \log_{10}\,M_0 + \beta\,; \qquad b = \gamma \cdot \log_{10}\,M_0 + \delta; \tag{4}$$

yielding $\alpha = -0.0905$; $\beta = 1.982$; $\gamma = -\,0.307$ and $\delta = -\,21.028$, where M_0 is in dyn× cm. Then, by combining (3) and (4),

$$\log_{10}\,Z = [\,\alpha \cdot \log_{10}\,M_0 + \beta\,] \cdot |\sin\,\Phi| + [\,\gamma \cdot \log_{10}\,M_0 + \delta\,]. \tag{5}$$

This represents an approximation, usable in the time domain, of the true directivity function (2), expressed in the frequency domain as a function of M_0 and ϕ. While it remains empirical, it is based on best fitting an extensive data set of theoretical solutions.

The combination of the distance correction expressing geometrical spreading on the sphere and of the effect of directivity leads to the formula

$$\log_{10}\,\eta = \log_{10}\,M_0\ -\ 0.5\,\log_{10}\,\sin\,\Delta + \left[\alpha \cdot \log_{10}\,M_0 + \beta\right] \cdot |\sin\,\Phi| + [\,\gamma \cdot \log_{10}\,M_0 + \delta\,], \tag{6}$$

where M_0 is in dyn×cm and η in metres. Note the presence of the two negative coefficients α and γ in (6), which express the destructive interference resulting from source finiteness and illustrated in the right-hand portion of Fig. 4.

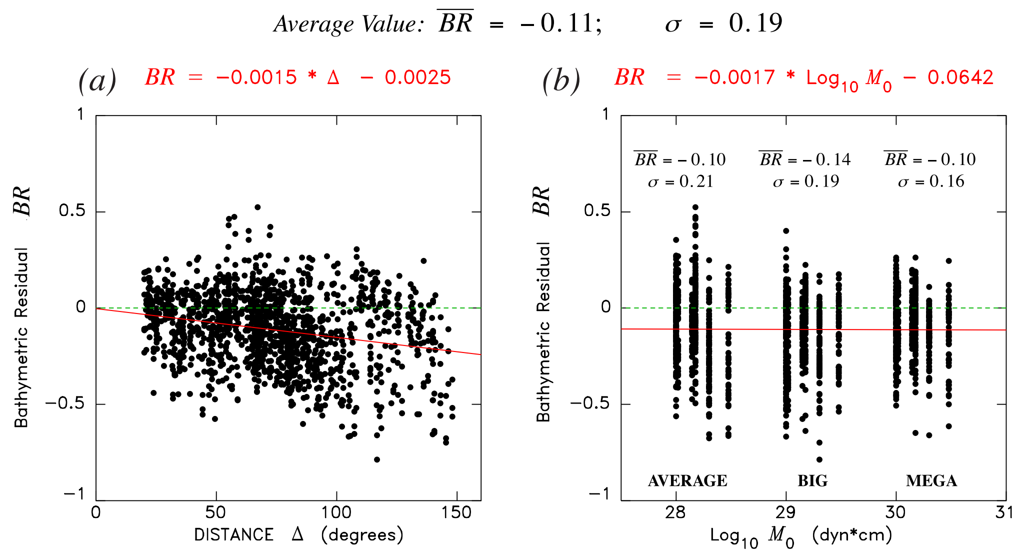

Figure 8. Bathymetric residual *BR* between amplitudes computed under Models 'Real' and '4000'. See text for details of computation. (a) Variation as a function of distance. Note the slight dependence on Δ, regressed as the solid red line. (b) Variation as a function of moment. Means and standard deviations are calculated for each group. Note absence of systematic dependence on M_0, but decrease of σ for larger events.

3.3 Performance of eq. (6) in the flat ocean

In order to evaluate the performance of eq. (6), we compute the logarithmic residuals

$$\mathrm{Res}_{4000} = \log_{10}\,\eta_{(\mathrm{Computed;\ 4000})} - \log_{10}\,\eta_{(6)}, \tag{7}$$

between values of η from our database of actual simulations, and predicted from (6), for the 1538 geometries corresponding to 'AVERAGE', 'BIG' and 'MEGA' sources. We exclude the 'SMALL' sources from that evaluation, since they are not significantly affected by directivity. We also exclude receivers at distances $\Delta < 20^\circ$, as the interference pattern is poorly represented by eq. (2), especially for the larger sources. The data set of Res_{4000} values is plotted as a function of $|\sin\Phi|$ in Fig. 7; it features an essentially null mean (less than 0.01 logarithmic units) and a standard deviation of only 0.11 logarithmic units, this low value indicating that (6) provides an acceptable match to the data set of simulated amplitudes in the flat basin model.

4 SIMULATIONS UNDER REAL BATHYMETRY

In order to proceed along a theoretically justifiable thread, the above results were obtained in the idealized framework of Model 4000, featuring a perfectly flat ocean floor with no continents or islands. We now extend our approach to simulations performed under a realistic bathymetric model of the Pacific Basin.

4.1 Correction for receiver bathymetry

We use an actual model (hereafter Model 'Real') of the bathymetry of the Pacific Ocean derived from Smith & Sandwell (1997). The locations of the receiving virtual gauges now correspond to various depths of water column, and hence are not directly comparable. For the purpose of estimating the effect of receiver bathymetry on η, we invoke Green's (1837) Law, which states that the conservation of energy flux for a wave in a water column whose depth H varies slowly along the direction of propagation requires the amplitude η to satisfy

$$\eta \cdot H^{1/4} = \mathrm{cnst.} \tag{8}$$

This expression is valid under the shallow water approximation, and strictly speaking for structures with transverse translational symmetry (Mei 1989). In this framework, we correct the amplitudes simulated at the 57 gauges under Real bathymetry by reverting them to a common depth of 4000 m through

$$\eta_{G\_\mathrm{Corr.}} = \eta_{(\mathrm{Computed;\ Real})} \cdot \left(\frac{H}{H_{4000}}\right)^{\frac{1}{4}}. \tag{9}$$

Once this correction has been effected, it becomes possible to compare the resulting $\eta_{G\_\mathrm{Corr.}}$ to the values simulated under Model 4000 at the same virtual gauge, $\eta_{(\mathrm{Computed;\ 4000})}$. Any difference between the two represents the effect (focusing and defocusing) of propagation over irregular bathymetry. For this purpose, we study in Fig. 8 the 'Bathymetric Residual':

$$BR = \log_{10}\,\eta_{G\_\mathrm{Corr.}} - \log_{10}\,\eta_{(\mathrm{Computed;\ 4000})}. \tag{10}$$

We suppress from this comparison geometries where the great circle from source to receiver intersects continental masses over a large distance (e.g. from Kuriles, Alaska or Cascadia to and from South America). Over such paths, the simulation code would compute a wave diffracted around the continental masses for Model 'Real', but propagating along the great circle for Model '4000', and the ratio of the two amplitudes is no longer representative of a simple focusing effect.

The mean value of the residuals in Fig. 8, $\overline{BR} = -0.11$ logarithmic units, suggests that the effect of bathymetry is generally defocusing, but its standard deviation, $\sigma_{BR} = 0.19$, greater than the absolute value of the mean, indicates that this is not a universal property.

Fig. 8(a) shows that in general, the negative effect of bathymetry increases (in absolute value) with distance. This is easily interpreted since a focusing effect (which increases amplitudes) is only a local phenomenon taking place in a limited range of distances (except under special circumstances such as propagation over long distances along a continuous mid-oceanic ridge), while defocusing generally

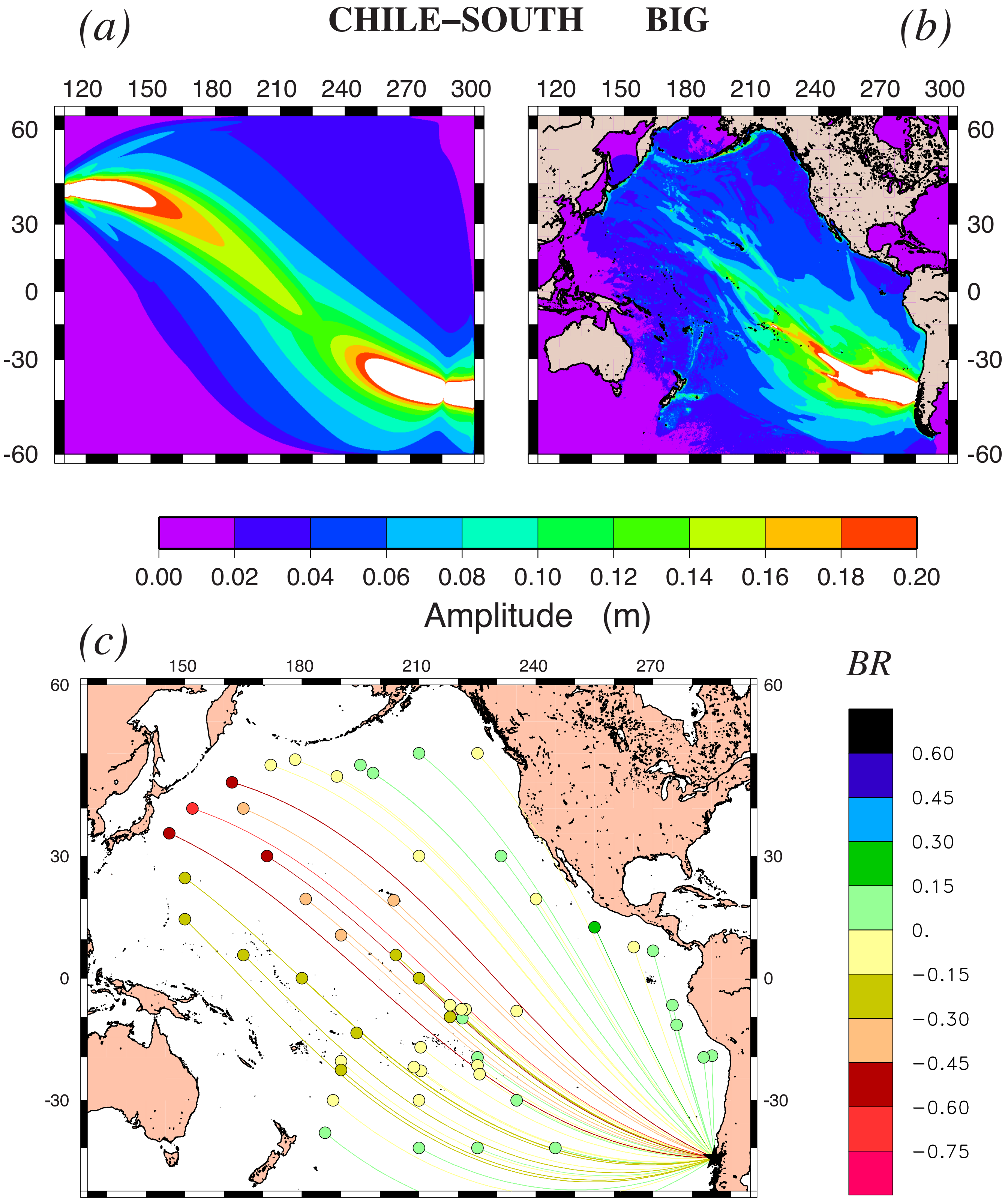

Figure 9. Comparison of amplitudes obtained under Models 4000 (a) and Real (b) in the case of the BIG source in region 9 (Chile-South). Note the refocusing towards the antipodes of the source in (a), which is absent from (b). (c) Individual great circle paths to 53 virtual gauges, colour-coded as a function of the value of the bathymetric residual *BR*, defined by (10). Note that the most deficient paths are those reaching close to the antipodes, where refocusing expected under Model 4000 is prevented by the irregular Real bathymetry.

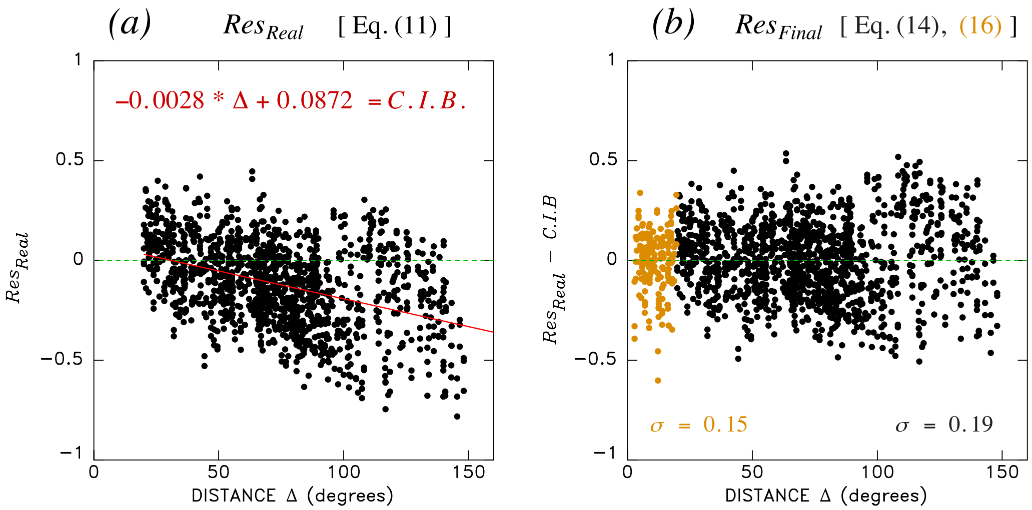

Figure 10. (a) Residual $\mathrm{Res}_{\mathrm{Real}}$ obtained by subtracting the logarithmic amplitude simulated (eq. 11) under Real bathymetry (corrected for Green's Law) from that predicted by eq. (6). The linear trend (solid red line) defines the correction for irregular bathymetry (C.I.B.). (b) Same as (a) after application of the C.I.B. Also shown in brown is the residual (16) in the near field ($\Delta < 20°$).

Table 2. Data set of DART Buoy records used in this study.

Date of event	Earthquake source				DART receiver				Δ	Φ	η	ζ	*Res*
D M (J) Y	Lat. (°)	Lon. (°)	M_0 (10^{27} dyn×cm)	ϕ_f (°)	ID	Lat. (°)	Lon. (°)	Depth (m)	(°)	(°)	(cm)	(cm)	
04 October (277) 1994	43.60	147.63	30.0	50	5700	54.29	−158.54	1760	36.0	87	1.9	0.9	−0.36
04 October (277) 1994	43.60	147.63	30.0	50	5900	54.04	−158.75	4814	35.9	86	1.5	1.0	−0.19
04 October (277) 1994	43.60	147.63	30.0	50	6000	54.02	−155.73	4728	37.7	86	1.5	1.0	−0.19
04 October (277) 1994	43.60	147.63	30.0	50	6100	45.96	−129.96	1629	55.9	84	1.5	1.5	0.00
04 October (277) 1994	43.60	147.63	30.0	50	6200	45.95	−130.00	1527	55.9	84	1.5	1.5	0.01
30 July (211) 1995	−24.17	−70.74	12.1	354	6900	45.93	−129.98	1527	88.2	59	0.8	0.9	0.08
10 June (162) 1996	51.10	−177.41	8.2	248	6700	45.96	−129.97	1590	31.3	78	1.0	0.8	−0.14
10 June (162) 1996	51.10	−177.41	8.2	248	7100	53.42	−157.28	4637	12.5	87	1.6	0.5	−0.50
10 June (162) 1996	51.10	−177.41	8.2	248	7200	52.04	−158.75	4551	11.6	80	1.7	0.7	−0.38
10 June (162) 1996	51.10	−177.41	8.2	248	7300	52.02	−155.72	4644	13.5	80	1.5	0.7	−0.36
17 November (321) 2003	51.14	177.86	5.3	280	1710	46.63	−170.79	5625	8.7	73	1.7	2.0	0.08
03 May (123) 2006	−20.39	−173.47	11.2	226	51407	19.63	−156.52	4712	43.2	68	0.8	1.3	0.19
03 May (123) 2006	−20.39	−173.47	11.2	226	0	20.51	−158.11	4626	43.5	65	0.9	1.0	0.08
03 May (123) 2006	−20.39	−173.47	11.2	226	46406	−8.49	−125.01	4421	48.2	53	0.9	0.7	−0.12
15 November (319) 2006	46.71	154.33	35.1	215	21414	48.94	178.27	5473	16.2	52	4.2	4.5	0.03
15 November (319) 2006	46.71	154.33	35.1	215	32401	−19.55	−74.81	5049	131.8	52	1.0	2.9	0.44
15 November (319) 2006	46.71	154.33	35.1	215	46402	51.07	−164.01	4727	27.4	60	2.5	2.5	0.02
15 November (319) 2006	46.71	154.33	35.1	215	46405	42.90	−130.91	3554	51.2	60	1.7	2.2	0.11
15 November (319) 2006	46.71	154.33	35.1	215	46408	48.63	−168.87	5247	24.7	53	2.8	4.4	0.21
15 November (319) 2006	46.71	154.33	35.1	215	46409	55.30	−148.50	4220	36.0	70	1.9	3.1	0.21
15 November (319) 2006	46.71	154.33	35.1	215	46411	39.34	−127.01	4318	55.6	58	1.6	2.7	0.23
15 November (319) 2006	46.71	154.33	35.1	215	46412	32.25	−120.70	3784	64.0	55	1.5	1.7	0.04
15 November (319) 2006	46.71	154.33	35.1	215	46413	48.67	−174.59	5372	20.9	52	3.1	4.7	0.18
15 November (319) 2006	46.71	154.33	35.1	215	46419	48.76	−129.62	2738	49.1	67	1.7	2.4	0.14
15 November (319) 2006	46.71	154.33	35.1	215	51406	−8.49	−125.01	4421	89.8	23	2.2	2.7	0.09
15 November (319) 2006	46.71	154.33	35.1	215	51407	19.63	−156.52	4712	48.2	18	3.6	3.4	−0.03
13 January (013) 2007	46.17	154.80	17.8	266	21413	30.55	152.12	6006	15.8	13	6.2	2.1	−0.47
13 January (013) 2007	46.17	154.80	17.8	266	21414	48.94	178.27	5473	16.0	76	2.1	2.9	0.14
13 January (013) 2007	46.17	154.80	17.8	266	46403	52.65	−156.94	4530	31.5	64	1.4	1.4	−0.01
13 January (013) 2007	46.17	154.80	17.8	266	46408	48.63	−168.87	5247	24.5	75	1.4	2.3	0.21
13 January (013) 2007	46.17	154.80	17.8	266	46409	55.30	−148.50	4220	36.0	58	1.4	0.6	−0.37
13 January (013) 2007	46.17	154.80	17.8	266	46410	57.63	−143.80	3755	38.2	54	1.5	1.0	−0.16
13 January (013) 2007	46.17	154.80	17.8	266	46411	39.34	−127.01	4318	55.6	71	0.9	0.5	−0.24
13 January (013) 2007	46.17	154.80	17.8	266	46412	32.25	−120.70	3784	63.9	74	0.9	1.0	0.06
13 January (013) 2007	46.17	154.80	17.8	266	46413	48.67	−174.59	5372	20.8	76	1.6	2.9	0.26
13 January (013) 2007	46.17	154.80	17.8	266	46419	48.76	−129.62	2738	49.1	62	1.2	1.0	−0.07
13 January (013) 2007	46.17	154.80	17.8	266	51407	19.63	−156.52	4712	47.7	69	1.0	0.8	−0.10
13 January (013) 2007	46.17	154.80	17.8	266	42402	51.07	−164.01	4787	27.4	69	1.4	0.4	−0.52

Table 2. *(Continued.)*

Date of event	Earthquake source				DART receiver				Δ	Φ	η	ζ	*Res*
D M (J) Y	Lat. (°)	Lon. (°)	M_0 (10^{27} dyn×cm)	ϕ_f (°)	ID	Lat. (°)	Lon. (°)	Depth (m)	(°)	(°)	(cm)	(cm)	
13 January (013) 2007	46.17	154.80	17.8	266	52405	12.88	132.33	5932	38.3	41	1.6	0.8	−0.31
01 April (091) 2007	−7.79	156.34	15.7	333	52402	11.74	154.22	5841	19.6	69	1.6	0.5	−0.50
01 April (091) 2007	−7.79	156.34	15.7	333	52403	4.03	145.60	4384	15.9	74	2.1	0.5	−0.62
15 August (227) 2007	−13.73	−77.04	11.2	321	32401	−19.55	−74.81	5049	6.2	71	3.6	4.5	0.10
15 August (227) 2007	−13.73	−77.04	11.2	321	32411	4.92	−90.68	3295	23.0	88	1.2	0.8	−0.19
15 August (227) 2007	−13.73	−77.04	11.2	321	43412	16.03	−107.00	3378	41.9	83	0.8	0.8	−0.01
15 August (227) 2007	−13.73	−77.04	11.2	321	46412	32.25	−120.70	3784	62.0	87	0.6	0.4	−0.20
15 August (227) 2007	−13.73	−77.04	11.2	321	51406	−8.49	−125.01	4421	47.3	40	1.1	1.0	−0.07
12 September (255) 2007	−3.78	100.99	68.0	328	23401	8.90	88.54	3469	17.7	77	5.0	1.8	−0.44
14 November (318) 2007	−22.64	−70.62	4.8	358	32401	−19.55	−74.81	5049	5.0	39	3.7	1.8	−0.32
14 November (318) 2007	−22.64	−70.62	4.8	358	32412	−17.98	−86.39	4446	15.5	17	2.6	0.9	−0.46
15 January (015) 2009	47.02	155.40	1.5	203	21413	30.55	152.12	6006	16.6	77	0.4	0.5	0.12
15 January (015) 2009	47.02	155.40	1.5	203	46408	49.63	−169.87	5247	23.1	42	0.5	0.6	0.12
15 January (015) 2009	47.02	155.40	1.5	203	46413	48.67	−174.59	5372	20.1	39	0.5	0.6	0.09
19 March (078) 2009	−23.10	−174.27	3.4	206	51425	−9.49	−176.24	5189	13.7	56	1.0	0.4	−0.39
19 March (078) 2009	−23.10	−174.27	3.4	206	51426	−22.99	−168.10	5698	5.7	26	3.5	2.9	−0.08
15 July (196) 2009	−45.81	166.28	6.0	22	55015	−46.92	160.56	5043	4.1	40	4.9	5.9	0.08
29 September (272) 2009	−15.19	−171.90	18.2	129	43412	16.03	−107.00	3378	71.2	28	1.5	2.6	0.22
29 September (272) 2009	−15.19	−171.90	18.2	129	51406	−8.49	−125.01	4421	46.3	48	1.3	1.1	−0.09
29 September (272) 2009	−15.19	−171.90	18.2	129	51425	−9.49	−176.24	5189	7.1	76	4.3	3.2	−0.13
29 September (272) 2009	−15.19	−171.90	18.2	129	51426	−22.99	−168.10	5698	8.6	63	4.1	6.9	0.23
07 October (280) 2009	−11.48	166.05	6.5	339	55012	−15.80	158.50	3150	8.5	10	6.8	3.8	−0.25
07 October (280) 2009	−11.48	166.05	6.5	339	51425	−9.49	−176.24	5189	17.5	16	2.8	0.7	−0.62
27 February (058) 2010	−35.95	−73.15	184.0	18	21413	30.55	152.12	6006	142.1	13	6.9	8.3	0.08
27 February (058) 2010	−35.95	−73.15	184.0	18	32412	−17.98	−86.39	4446	21.4	35	12.3	16.5	0.13
27 February (058) 2010	−35.95	−73.15	184.0	18	43412	16.03	−107.00	3378	60.9	34	6.8	8.7	0.11
27 February (058) 2010	−35.95	−73.15	184.0	18	46403	52.65	−156.94	4530	114.3	30	4.8	4.9	0.01
27 February (058) 2010	−35.95	−73.15	184.0	18	46404	45.86	−128.78	2517	95.8	36	5.2	3.3	−0.20
27 February (058) 2010	−35.95	−73.15	184.0	18	46409	55.30	−148.50	4220	111.3	35	4.4	5.9	0.13
27 February (058) 2010	−35.95	−73.15	184.0	18	51406	−8.49	−125.01	4421	54.5	1	15.8	19.5	0.09
27 February (058) 2010	−35.95	−73.15	184.0	18	51425	−9.49	−176.24	5189	94.9	34	4.7	3.3	−0.15
27 February (058) 2010	−35.95	−73.15	184.0	18	51426	−22.99	−168.10	5698	80.6	40	4.4	4.2	−0.02
27 February (058) 2010	−35.95	−73.15	184.0	18	52401	19.27	155.77	5646	134.1	26	5.0	7.9	0.20
27 February (058) 2010	−35.95	−73.15	184.0	18	52402	11.74	154.22	5841	131.0	36	3.9	4.3	0.04
27 February (058) 2010	−35.95	−73.15	184.0	18	52403	4.03	145.60	4384	132.2	51	3.2	4.6	0.17
27 February (058) 2010	−35.95	−73.15	184.0	18	52405	12.88	132.33	5932	147.5	57	2.8	4.4	0.19
25 October (298) 2010	−3.49	100.08	6.8	316	56001	−13.99	110.01	5660	14.3	89	1.2	2.4	0.30
11 March (070) 2011	38.32	142.97	400.0	193	21401	42.62	152.58	5263	8.5	46	38.9	44.2	0.05
11 March (070) 2011	38.32	142.97	400.0	193	21413	30.51	152.12	6006	10.9	30	42.7	54.5	0.10
11 March (070) 2011	38.32	142.97	400.0	193	21414	48.94	178.28	5473	27.4	47	12.9	17.0	0.12
11 March (070) 2011	38.32	142.97	400.0	193	21415	50.18	171.85	4772	23.7	52	13.2	20.9	0.20
11 March (070) 2011	38.32	142.97	400.0	193	21419	44.46	155.74	5318	11.4	50	29.5	38.1	0.11
11 March (070) 2011	38.32	142.97	400.0	193	32401	−19.29	−74.73	5049	142.2	33	7.4	9.8	0.12
11 March (070) 2011	38.32	142.97	400.0	193	32412	−17.98	−86.39	4446	132.6	25	9.1	10.2	0.05
11 March (070) 2011	38.32	142.97	400.0	193	32413	−7.40	−93.50	3890	120.7	29	8.3	13.8	0.22
11 March (070) 2011	38.32	142.97	400.0	193	43412	16.03	−107.00	3378	95.1	38	7.8	11.1	0.16
11 March (070) 2011	38.32	142.97	400.0	193	43413	11.06	−99.85	3521	103.5	39	7.1	17.0	0.38
11 March (070) 2011	38.32	142.97	400.0	193	46402	51.07	−164.02	4727	38.9	50	10.0	10.9	0.03
11 March (070) 2011	38.32	142.97	400.0	193	46403	52.64	−156.93	4530	43.2	53	9.1	10.1	0.05
11 March (070) 2011	38.32	142.97	400.0	193	46404	45.86	−128.77	2517	62.6	51	8.3	13.0	0.19
11 March (070) 2011	38.32	142.97	400.0	193	46408	49.63	−169.87	5247	35.2	47	11.0	14.0	0.10
11 March (070) 2011	38.32	142.97	400.0	193	46409	55.30	−148.49	4220	47.8	57	7.9	7.7	−0.02
11 March (070) 2011	38.32	142.97	400.0	193	46410	57.63	−143.80	3755	49.9	61	7.6	6.5	−0.07
11 March (070) 2011	38.32	142.97	400.0	193	46411	39.33	−127.01	4318	67.0	46	7.8	16.2	0.32
11 March (070) 2011	38.32	142.97	400.0	193	51406	−8.48	−125.03	4421	96.8	8	15.5	17.4	0.05
11 March (070) 2011	38.32	142.97	400.0	193	51407	19.64	−156.52	4712	55.1	11	20.0	24.3	0.09
11 March (070) 2011	38.32	142.97	400.0	193	51425	−9.49	−176.24	5189	61.0	29	11.2	10.9	−0.01
11 March (070) 2011	38.32	142.97	400.0	193	52402	11.88	154.12	5841	28.2	53	11.2	28.0	0.40
11 March (070) 2011	38.32	142.97	400.0	193	52403	4.03	145.60	4384	34.3	72	8.3	10.1	0.09
11 March (070) 2011	38.32	142.97	400.0	193	52405	12.88	132.33	5932	27.1	80	8.5	6.7	−0.10
11 March (070) 2011	38.32	142.97	400.0	193	52406	−5.30	165.01	2288	48.1	47	11.2	14.2	0.11
11 March (070) 2011	38.32	142.97	400.0	193	54401	−33.01	−172.99	5877	82.1	41	6.9	3.3	−0.32
11 April (102) 2012	2.35	92.82	91.4	289	23401	8.90	88.54	3469	7.8	52	16.2	5.0	−0.51

Table 2. (*Continued.*)

Date of event	Earthquake source				DART receiver				Δ	Φ	η	ζ	*Res*
D M (J) Y	Lat. (°)	Lon. (°)	M_0 (10^{27} dyn×cm)	ϕ_f (°)	ID	Lat. (°)	Lon. (°)	Depth (m)	(°)	(°)	(cm)	(cm)	
11 April (102) 2012	2.35	92.82	91.4	289	56001	−13.99	110.01	5660	23.6	65	4.4	1.0	−0.64
11 April (102) 2012	0.90	92.31	28.9	107	23401	8.90	88.54	3469	8.8	42	8.3	3.0	−0.44
11 April (102) 2012	0.90	92.31	28.9	107	56001	−13.99	110.01	5660	23.0	66	2.1	1.0	−0.33
28 October (302) 2012	52.61	−132.06	5.7	318	46402	42.60	231.10	4727	10.2	61	1.8	3.0	0.23
28 October (302) 2012	52.61	−132.06	5.7	318	46403	52.65	−156.94	4530	15.1	52	1.4	3.0	0.32
28 October (302) 2012	52.61	−132.06	5.7	318	46404	45.86	−128.78	2517	7.1	67	2.6	5.0	0.29
28 October (302) 2012	52.61	−132.06	5.7	318	46407	42.60	231.10	3244	10.2	61	1.9	7.5	0.58
28 October (302) 2012	52.61	−132.06	5.7	318	46408	49.63	−169.87	5247	23.7	50	1.0	2.0	0.32
28 October (302) 2012	52.61	−132.06	5.7	318	46409	55.30	−148.50	4220	10.0	64	1.8	3.5	0.29
28 October (302) 2012	52.61	−132.06	5.7	318	46410	57.63	−143.80	3755	8.4	83	1.9	2.0	0.03
28 October (302) 2012	52.61	−132.06	5.7	318	46411	39.34	−127.01	4318	13.7	65	1.3	5.0	0.57
28 October (302) 2012	52.61	−132.06	5.7	318	46419	48.76	−129.62	2738	4.2	71	3.5	7.5	0.33
06 February (037) 2013	−11.08	165.14	8.6	314	52406	−5.33	165.09	2288	5.7	45	5.5	8.5	0.19
06 February (037) 2013	−11.08	165.14	8.6	314	55012	−15.80	158.40	3150	8.1	10	8.7	13.3	0.19
06 February (037) 2013	−11.08	165.14	8.6	314	55023	−14.80	153.58	4595	11.9	27	3.9	5.0	0.11

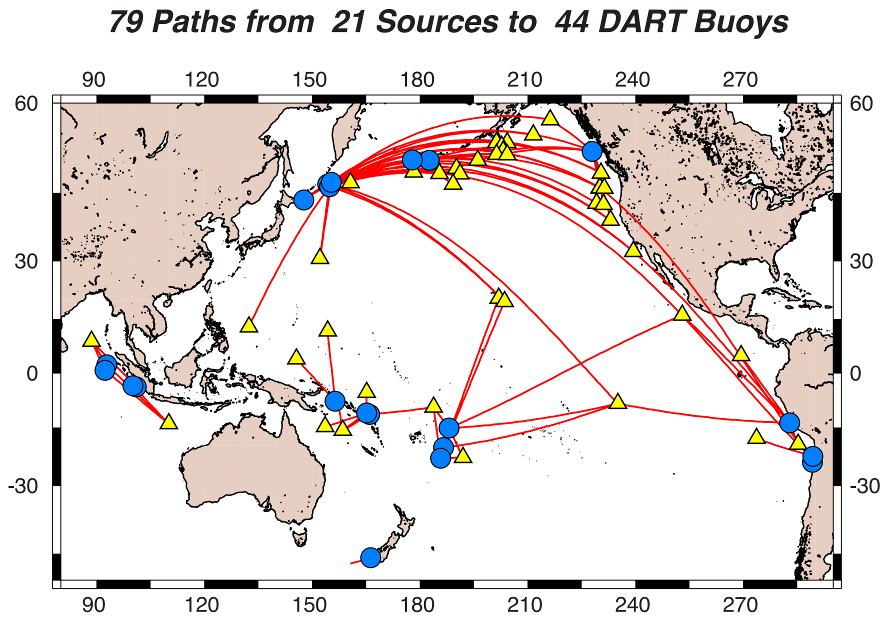

Figure 11. Map of the events (circles), receivers (triangles) and paths used in the study of the DART buoy records. The 2010 Maule and 2011 Tohoku data sets are presented in Fig. 12.

disperses energy in a more permanent fashion.[1] As a result, the longer the distance Δ travelled, the more exposed the wave will be to the effect of irregular bathymetry, which in turn has a greater chance of being destructive; hence a negative dependence of *BR* on Δ.

In Fig. 8(b), we similarly explore any possible dependence of *BR* on seismic moment M_0. While we detect no systematic trend, we note a decrease of the standard deviations σ with increasing moment. This probably illustrates the fact that 'MEGA' events are expected to feature longer wavelengths, which would be less sensitive to variations in bathymetry than their shorter counterparts generated by smaller sources.

The behaviour of *BR* is detailed in the case of the 'BIG' source in Region 'CHILE-SOUTH' in Fig. 9. Frame (a), which maps the simulation under Model 4000, features the strong directivity resulting from source finiteness, directed towards Japan, at right angles from fault strike. Note however that the strong amplitudes found in the NW part of the domain are due to refocusing under geometrical spreading at the antipodes of the source. This effect requires a perfect coherence in phase among rays travelling at different azimuths, and thus will not take place under an irregular bathymetry, as clearly shown in Fig. 9(b), obtained under Model 'Real'. Finally, Fig. 9(c) maps colour-coded values of *BR* for individual rays to 53 virtual gauges, confirming that, in this particular case, the only significantly deficient values of *BR* express the lack of antipodal refocusing for the longest paths inside the lobe of directivity.

Finally, in Fig. 10, we study the performance of (6) as a predictor of tsunami amplitude under Model 'Real' by forming the residual

$$\mathrm{Res}_{\mathrm{Real}} = \log_{10}\,\eta_{G\_\mathrm{Corr.}} - \log_{10}\,\eta_{(6)}. \qquad (11)$$

---

[1] This can be compared to the case of rays emerging from a convergent lens in geometrical optics, which will be amplified only up to the lens' focus, and will diverge thereafter. On the opposite, rays emerging from a divergent lens will be defocused in the entire space beyond it.

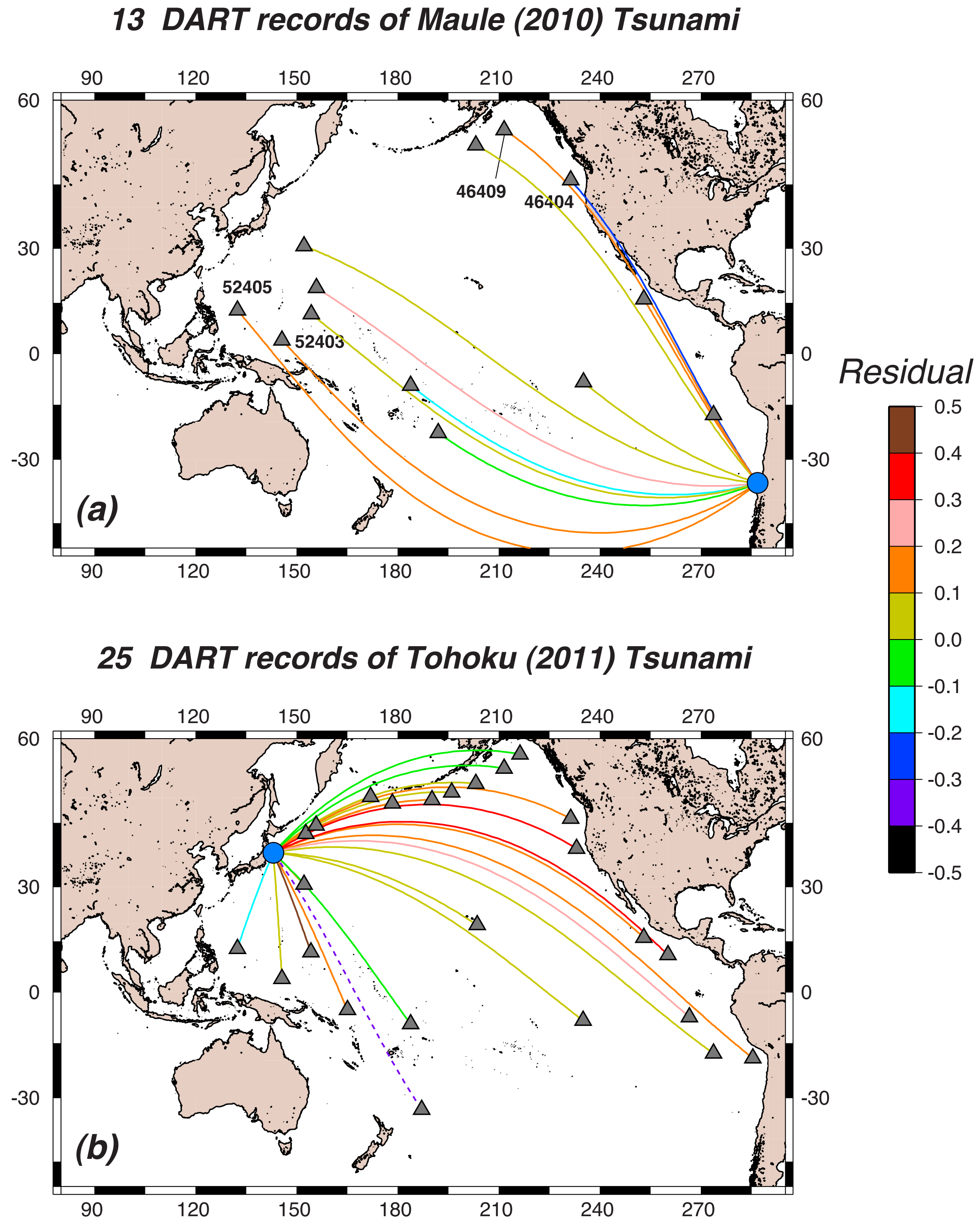

Figure 12. Same as Fig. 11 for the 2010 Maule, Chile (a) and 2011 Tohoku, Japan (b) tsunamis. Each path has been colour-coded according to the value of the residual $\mathrm{Res}_{\mathrm{DART}}$. Buoys whose records are discussed in the text are identified by their NOAA numbers. In (b), the dashed line shows the path to Buoy 54401, whose datum remains tentative, as it did not trigger into detection mode.

The mean value $\overline{\mathrm{Res}_{\mathrm{Real}}} = -0.12$ remains very small, and comparable to $\overline{BR}$ since (11) is the exact combination of (7) and (10). Similarly, the standard deviation of $\mathrm{Res}_{\mathrm{Real}}$, 0.21 logarithmic unit, is dominated by that of BR (0.19). Fig. 10(a) shows that $\mathrm{Res}_{\mathrm{Real}}$ increases (in absolute value) regularly with Δ, as greater distances result in a greater effect of irregular bathymetry. A linear regression yields

$$\langle \mathrm{Res}_{\mathrm{Real}} \rangle = -0.0028\,\Delta + 0.0872 = \mathrm{C.I.B.}, \tag{12}$$

(Δ in degrees), which defines a 'Correction for Irregular Bathymetry (hereafter C.I.B.)', to be added to the value of η given by (6).

A final expression for the amplitude η expected at a virtual gauge located at a distance Δ in the azimuth ϕ_s ($\Phi = \phi_f - \phi_s - \pi/2$) in water of depth H is therefore

$$\begin{aligned}\log_{10} \eta_{\mathrm{Final}} = {} & \log_{10} M_0 \;-\; 0.5 \log_{10} \sin \Delta \;-\; 0.0028\,\Delta \\ & + [\,\alpha \cdot \log_{10} M_0 \;+\; \beta\,] \cdot |\sin \Phi\,| \\ & + [\,\gamma \cdot \log_{10} M_0 \;+\; \delta'\,] - \frac{1}{4} \log_{10} \left(\frac{H}{H_{4000}} \right),\end{aligned} \tag{13}$$

with a new constant $\delta' = -20.941$. The performance of this final formula is explored in Fig. 10(b) by computing a final residual

$$\mathrm{Res}_{\mathrm{Final}} = \log_{10} \eta_{\mathrm{Real}} \;-\; \log_{10} \eta_{\mathrm{Final}} = \mathrm{Res}_{\mathrm{Real}} \;-\; \mathrm{C.I.B.}, \tag{14}$$

where $\eta_{\rm Final}$ is computed using (13). The average value of $\mathrm{Res}_{\rm Final}$ is obviously zero, while its standard deviation remains $\sigma = 0.19$ logarithmic unit,

At distances shorter than 20°, the effect of source finiteness does not lend itself to representation by a formula of the type (2), which tacitly assumes an infinite distance. In addition to the effect of geometrical spreading, parameters such as distance Δ, azimuth Φ and moment M_0 (through its effect on fault length L) are expected to contribute through destructive interference to reduced amplitudes η. In this context we model this effect empirically by regressing a data set of 171 AVERAGE, BIG and MEGA amplitudes simulated in Real bathymetry (once scaled by M_0 and corrected for geometrical spreading and receiver bathymetry) as a function of Δ, $|\sin\Phi|$ and $\log_{10} M_0$. We found that the expression

$$\begin{aligned}\log_{10}\eta_{\rm Near} &= \log_{10} M_0 - 0.5\log_{10}\sin\Delta \\ &\quad - 0.0137\,\Delta - 0.6263\,|\sin\Phi| - 0.3531 \\ &\quad \times \log_{10} M_0 - 19.372 - \frac{1}{4}\log_{10}\left(\frac{H}{H_{4000}}\right)\end{aligned} \tag{15}$$

minimizes the residuals

$$\mathrm{Res}_{\Delta<20} = \log_{10}\eta_{\rm (Computed;Real)} - \log_{10}\eta_{\rm Near;(15)} \tag{16}$$

in the field $\Delta < 20°$ with a standard deviation $\sigma = 0.15$ units which compares favourably with that of the residuals (14). The corresponding points are plotted in brown in Fig. 10(b).

5 APPLICATION TO ACTUAL DART BUOY RECORDS, 1994–2013

In this section, we compare the amplitudes predicted by (13) [or (15)] to 116 values actually recorded by DART buoys during a selection of tsunamis of the past 20 yr, listed in Table 2. The paths sampled are plotted in Figs 11 and 12.

The use of DART records from the 2011 Tohoku event is particularly important for two reasons: First, their amplitudes are the largest ever recorded on DART buoys, and they allow testing our methodology for a domain of moments approaching the range of 'MEGA' sources; second, the event took place in a region which was not used for the development of our algorithm, and thus the Tohoku records provide an independent means of testing our methodology.

For each DART record, we define an amplitude ζ as one-half the maximum peak-to-peak deviation recorded by the buoy during the passage of the tsunami. We then compute the value η predicted by (13) [or (15) at distances less than 20°] and define a logarithmic residual for DART records

$$\mathrm{Res}_{\rm DART} = \log_{10}\zeta - \log_{10}\eta_{(13)\,[15]}. \tag{17}$$

These residuals, in the nature of 'observed minus computed' values, can serve to evaluate the performance of our methodology. Fig. 13 plots observed ζ against η forecast by eq. (13) (or eq. 15). We use special symbols for the following events: 2011 Tohoku (red triangles), 2010 Maule (green inverted triangles), 2009 Samoa (blue diamonds) and 2012 Indian Ocean (yellow squares). Open symbols correspond to distances shorter than 20°. The average value of the entire data set of residuals $\mathrm{Res}_{\rm DART}$ is a perfect 0.00 logarithmic unit, and its standard deviation σ, 0.25 logarithmic unit, or a multiplicative or divisive factor of 1.8. The data set of residuals $\mathrm{Res}_{\rm DART}$ is plotted against distance and moment in Fig. 14.

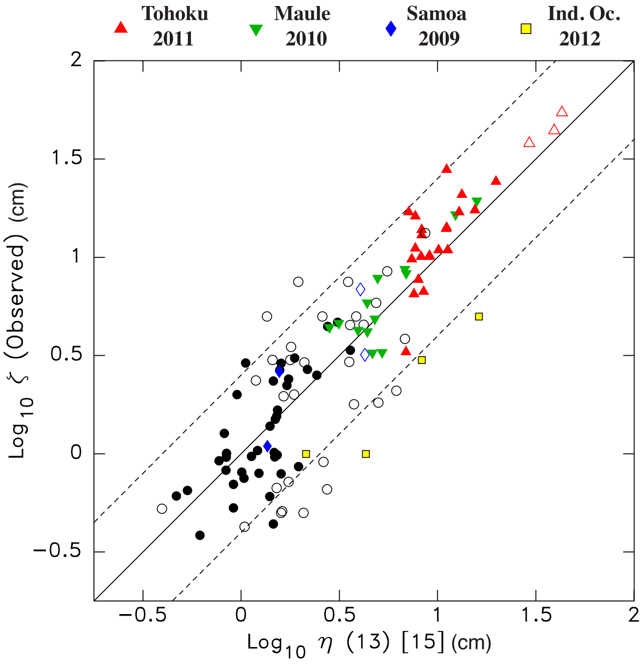

Figure 13. Amplitudes ζ recorded on DART buoys versus estimates η computed using (13) [or (15) for $\Delta < 20°$]. Special symbols are used for the 2009, 2010, 2011 and 2012 events, as discussed in the text. Open symbols correspond to distances less than 20°. The scales are logarithmic in units of centimetres. The dashed lines correspond to $\mathrm{Res}_{\rm DART} = \pm 0.4$ logarithmic units.

As shown in Figs 13 and 14, most of the scatter in residuals occurs at the shorter distances; indeed for $\Delta > 20°$, where η is computed using (13), σ falls to 0.20 while the average value of (17) remains 0.02. This poorer performance of (15) as compared to (13) is probably related to the influence, at short distance, of structural details in the seismic source, such as the distribution of seismic slip on the fault, which may affect tsunami amplitudes in the near field, but become largely irrelevant in the far field, which is increasingly controlled by the integral of the source. In the far field ($\Delta > 20°$), only two records have residuals $|\mathrm{Res}_{\rm DART}| > 0.4$ units: the Kuril interplate event of 2006 November 15 recorded at Buoy 32401 off the coast of Northern Chile ($\mathrm{Res}_{\rm DART} = 0.44$) and the Kuril Islands normal faulting event of 2007 January 13 recorded at Buoy 42402 off Unimak Island ($\mathrm{Res}_{\rm DART} = -0.52$). Furthermore, Fig. 14 illustrates the absence of any systematic trend in residual with either distance (beyond 20°) or seismic moment, thus validating the various corrections incorporated into (13) (and to a lesser extent, eq. 15).

Finally, a rather remarkable result of the data set listed in Table 2 and plotted in Fig. 13, is that even those events for which the modelled focal mechanism is clearly erroneous (1994 Kuril, 2007 Kuril and 2009 Samoa) do not lead to extravagant residuals.

5.1 Extension to areas not part of the simulation

The universal character of eqs (13) and (15) can be tested by examining the residuals obtained for tsunami sources located outside the regions targeted in the simulations used to build the relevant formulae. This is the case of the 2011 Tohoku tsunami, which contributes 25 DART records to our data set (shown as red symbols in Fig. 13). We find no systematic trend in residuals for the 2011 Tohoku event, which therefore serves to

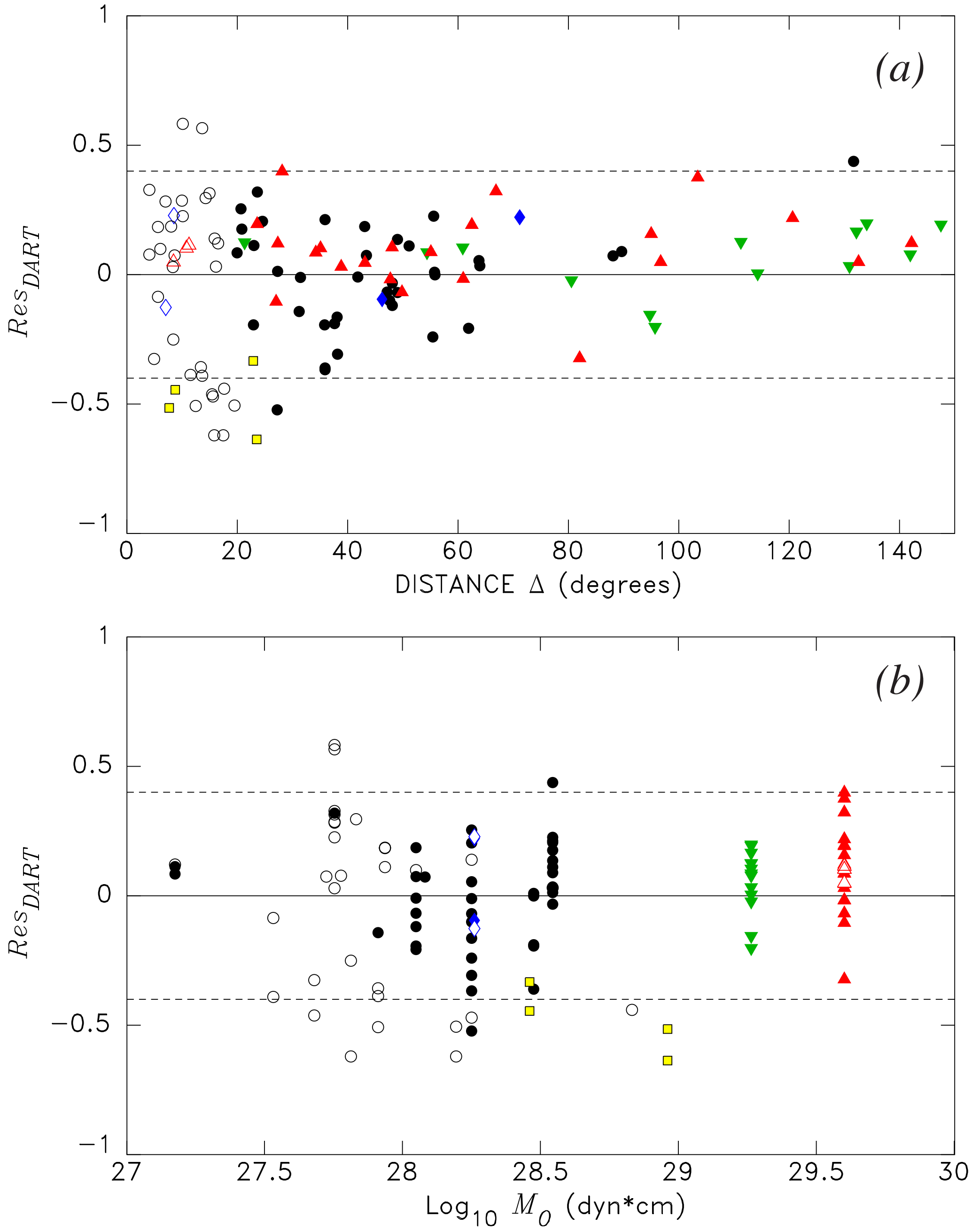

Figure 14. Residuals Res_{DART} plotted against distance (a) and seismic moment (b). Dashed lines and special symbols as in Fig. 13.

validate our approach outside of the specific regions used for our simulations.

In addition, and as mentioned in Fig. 11 and in Table 2, we use four Indian Ocean sources in our data set: The 2007 Bengkulu earthquake (Borrero *et al.* 2009), the 2010 Mentawai tsunami earthquake (Newman *et al.* 2011; Hill *et al.* 2012) and the two intraplate North Sumatra earthquakes of 2012 April 11 (Yue *et al.* 2012). Unfortunately, because of the sparse development of DART buoys in the Indian Ocean, these events contribute only six records: one each in 2007 and 2010, and two each for the 2012 events. The 2007 path is very short ($\Delta = 8.9°$) and the great circle arc intersects the Mentawai and Nias Islands; this could explain the strongly negative residual (−0.44). By contrast, the 2010 Mentawai record features a strong residual (+0.30) which could be due primarily to the nature of the source as a ‘tsunami earthquake’. At any rate, this residual remains within the mainstream of the scatter observed in our data set. As for the 2012 records, their systematically negative residuals (−0.33 to −0.64, shown as squares in Figs 13 and 14), reflect primarily the strike-slip nature of the sources, which generate systematically deficient tsunamis in the near to intermediate field.

5.2 2010 Maule records: a specific discussion

The 13 data recorded from the 2010 Maule tsunami are presented in Fig. 12(a), with the great-circle paths colour-coded according to the value of the residual Res_{DART}. The average residual is

$\mathrm{Res}_{\mathrm{Maule}} = 0.06 \pm 0.12$ logarithmic units, in itself an excellent result. In general, eq. (13) accurately predicts (to within 0.2 logarithmic units) the deep-sea amplitudes in the Central Pacific Basin. Surprisingly, this also includes paths intersecting complex structures such as the Fiji Plateau and Solomon Island Arc system (to Buoys 52403 and 52405 located in the Caroline and Philippine Seas), which feature positive residuals (+0.17 and +0.20); this suggests propagation outside the great circle arc, and thus emergence from the source closer to the lobe of directivity. Only the path to Buoy 46404 off the coast of Oregon, which requires a strong diffraction around the North American continent has a clearly deficient residual (−0.20), while that to Buoy 46409 is actually positive (+0.13), despite an essentially common great circle. These examples illustrate the subtle effects that actual bathymetry can produce on wave amplitude, notably when involving diffraction around continental masses.

5.3 2011 Tohoku records: a specific discussion

The 25 data recorded from the 2011 Tohoku tsunami are similarly presented in Fig. 12(b). The average residual is $\mathrm{Res}_{\mathrm{Tohoku}} = 0.10 \pm 0.15$ logarithmic units. The amplitudes to the Central Pacific, in the centre of the lobe of directivity, are correctly predicted (generally to within ±0.1 units), but we note a systematic trend towards underestimation of the amplitudes for paths sampling the Northeastern part of the Pacific Ocean towards the Western coasts of North America; only those paths for which the great circle penetrates the Bering Sea are clearly overestimated. This can be interpreted by noting that the 2011 Tohoku earthquake was a clear violator of seismic scaling laws, featuring a much greater slip (on the order of 50 m) concentrated an a small patch of fault plane, not exceeding 120 km (Lay *et al.* 2011). As a result, the directivity of the actual source should be weaker than predicted under the scaling laws used to build the various sources, which went into the development of eq. (13), the lobe of directivity should be broader, and consequently the wave amplitudes to the side of the lobe stronger than predicted using (13), in general agreement with our observations.

6 CONCLUSION

Based on theoretical arguments, we have established a formula (13) which can be used to predict amplitudes of tsunami waves in the far field ($\Delta > 20^\circ$). It incorporates the effects of seismic moment, geometrical spreading and Green's Law applied to correct for receiver bathymetry. The crucial effect of directivity due to source finiteness is best fit empirically to a combined function of moment and receiver azimuth. Finally, the effect of propagating over an irregular bathymetry is modelled as a linear function of distance. This algorithm accurately predicts the amplitudes of simulated waveforms with a standard deviation of only 0.19 logarithmic units.

In the near field, the effect of directivity can be modelled in an *ad hoc* fashion using a regression over distance, azimuth and moment. The resulting formula (15) fits simulated amplitudes with a standard deviation of 0.15 logarithmic units.

This algorithm successfully predicts amplitudes recorded on the high seas during the 2011 Tohoku tsunami, even though its epicentral region was not included in the development of formulae (13) and (15).

ACKNOWLEDGEMENTS

Benjamin Heath helped in the gathering and initial processing of the 2011 Tohoku DART data. Some of the figures were constructed using the GMT software (Wessel & Smith 1991).

REFERENCES

Ben-Menahem, A., 1961. Radiation of seismic surface-waves from finite moving sources, *Bull. seism. Soc. Am.,* **51,** 401–435.

Ben-Menahem, A. & Rosenman, M., 1972. Amplitude patterns of tsunami waves from submarine earthquakes, *J. geophys. Res.,* **77,** 3097–3128.

Borrero, J.C., Weiss, R., Okal, E.A., Hidayat, R., Suranto, Arcas, D. & Titov, V.V., 2009. The tsunami of 12 September 2007, Bengkulu Province, Sumatra, Indonesia: post-tsunami survey and numerical modeling, *Geophys. J. Int.,* **178,** 180–194.

Geller, R.J., 1976. Scaling relations for earthquake source parameters and magnitudes, *Bull. seism. Soc. Am.,* **66,** 1501–1523.

Gilbert, F., 1970. Excitation of the normal modes of the Earth by earthquake sources, *Geophys. J. R. astr. Soc.,* **22,** 223–226.

Green, G., 1837. On the motion of waves in a canal of variable depth, *Cam. Phil. Trans.,* **6,** 457–462.

Guibourg, S., Heinrich, P. & Roche, R., 1997. Numerical modeling of the 1995 Chilean tsunami: impact on French Polynesia, *Geophys. Res. Lett.,* **24,** 775–778.

Hébert, H., Heinrich, P., Schindelé, F. & Piatanesi, A., 2001. Far-field simulations of tsunami propagation in the Pacific Ocean: impact on the Marquesas Islands (French Polynesia), *J. geophys. Res.,* **106,** 9161–9177.

Hill, E.M. *et al.*, 2012. The 2010 $M_w = 7.8$ Mentawai earthquake: very shallow source of a rare tsunami earthquake determined from tsunami field survey and near-field GPS, *J. geophys. Res.,* **117**(B6), B06402, doi:10.1029/2012JB009159.

Lay, T., Ammon, C.J., Kanamori, H., Xue, L. & Kim, M.J., 2011. Possible large near-trench slip during the 2011 $M_w = 9.0$ off the Pacific coast of Tohoku earthquake, *Earth Planets Space,* **63,** 687–692.

McCaffrey, R., 2007. The next great earthquake, *Science,* **315,** 1675–1676.

Mei, C.C., 1989. *The Applied Dynamics of Ocean Surface Waves, Advances Series on Ocean Engineering,* Vol. **1,** 740 pp., World Scientific.

Newman, A.V., Hayes, G., Wei, Y. & Convers, J.A., 2011. The 25 October 2010 Mentawai tsunami earthquake, from real-time discriminants, finite-fault rupture, and tsunami excitation, *Geophys. Res. Lett.,* **38**(5), L05302, doi:10.1029/2010GL046498.

Okal, E.A., 1989. A theoretical discussion of time-domain magnitudes: the Prague formula for M_s and the mantle magnitude M_m, *J. geophys. Res.,* **94,** 4194–4204.

Okal, E.A. & Talandier, J., 1991. Single-station estimates of the seismic moment of the 1960 Chilean and 1964 Alaskan earthquakes, using the mantle magnitude M_m, *Pure appl. Geophys.,* **136,** 103–126.

Reymond, D., Okal, E.A., Hébert, H. & Bourdet, M., 2012. Rapid forecast of tsunami wave heights from a database of pre-computed simulations, and application during the 2011 Tohoku tsunami in French Polynesia, *Geophys. Res. Lett.,* **39**(11), L11603, doi:10.1029/2012/GL051640.

Ruff, L.J. & Kanamori, H., 1980. Seismicity and the subduction process, *Phys. Earth planet. Inter.,* **23,** 240–252.

Satake, K., 1987. Effects of bathymetry on tsunami propagation: application of ray tracing to tsunamis, *Pure appl. Geophys.,* **126,** 27–36.

Scholz, C.H., 1982. Scaling laws for large earthquakes: consequences for physical models, *Bull. seism. Soc. Am.,* **72,** 1–14.

Smith, W.H.F. & Sandwell, D.T., 1997. Global seafloor topography from satellite altimetry and ship depth soundings, *Science,* **277,** 1957–1962.

Stein, S. & Okal, E.A., 2007. Ultra-long period seismic study of the December 2004 Indian Ocean earthquake and implications for regional tectonics and the subduction process, *Bull. seism. Soc. Am.,* **97,** S279–S295.

Tadepalli, S. & Synolakis, C.E., 1996. Model for the leading wave of tsunamis, *Phys. Rev. Lett.,* **77,** 2141–2144.

Talandier, J. & Okal, E.A., 1989. An algorithm for automated tsunami warning in French Polynesia, based on mantle magnitudes, *Bull. seism. Soc. Am.,* **79,** 1177–1193.

Titov, V.V., González, F., Bernard, E., Eble, M., Mofjeld, H., Newman, J. & Venturato, A., 2005. Real-time tsunami forecasting: Challenges and solutions, *Nat. Hazards,* **35,** 35–41.

Ward, S.N., 1980. Relationships of tsunami generation and an earthquake source, *J. Phys. Earth,* **28,** 441–474.

Wessel, P. & Smith, W.H.F., 1991. Free software helps map and display data, *EOS, Trans. Am. geophys. Un.,* **72,** 441 and 445–446.

Woods, M.T. & Okal, E.A., 1987. Effect of variable bathymetry on the amplitude of teleseismic tsunamis: a ray-tracing experiment, *Geophys. Res. Lett.,* **14,** 765–768.

Yue, H., Lay, T. & Koper, K.D., 2012. En-échelon and orthogonal fault ruptures of the 11 April 2012 great intraplate earthquakes, *Nature,* **490,** 245–249.